Saturation dependence of mass transfer for solute transport through residual unsaturated porous media

Zhi Dou[a,b,*], Xueyi Zhang[a,c], Chao Zhuang[a], Yun Yang[a], Jinguo Wang[a], Zhifang Zhou[a]

[a] *School of Earth Science and Engineering, Hohai University, Nanjing, 210098 China*

[b] *Department of Civil Engineering, University of Toronto, 35 St. George Street, Toronto, ON M5S 1A4, Canada*

[c] *Eawag, Swiss Federal Institute of Aquatic Science and Technology, 8600 Dübendorf, Switzerland*

**Corresponding author: Zhi Dou*

E-mail: douz@hhu.edu.cn

This document is the accepted manuscript version of the following article:
Dou, Z., Zhang, X., Zhuang, C., Yang, Y., Wang, J., & Zhou, Z. (2022). Saturation dependence of mass transfer for solute transport through residual unsaturated porous media. International Journal of Heat and Mass Transfer, 188, 122595 (13 pp.). https://doi.org/10.1016/j.ijheatmasstransfer.2022.122595

This manuscript version is made available under the CC-BY-NC-ND 4.0 license http://creativecommons.org/licenses/by-nc-nd/4.0/

Abstract:

The residual non-wetting phase in unsaturated porous media varies the aqueous pore space due to the immiscible characteristics. The varied pore space in turn has significant influence on the mass transfer for aqueous tracer transport through residual unsaturated porous media. In this study, the mass transfer for solute transport through residual unsaturated porous media was investigated. A pore-scale numerical simulation (PSNS) model consisting of both immiscible two-phase flow transport and aqueous-miscible solute transport was developed at pore scale to capture the topology of residual saturation and the tempo-spatial evolution of aqueous tracer in residual unsaturated porous media. The results showed that as the immiscible fluid-fluid displacement pattern varied from compact displacement to capillary fingering, the residual saturation (S_{rw}) increased and the velocity spatial variability in the residual aqueous flow field was enhanced. Inversion of the advection-dispersion-equation (ADE) model and the continuous-time-random-walk (CTRW) model indicated the typical characteristics of anomalous aqueous tracer transport (i.e., early arrivals and long tails) in breakthrough curves (BTCs) in a range of S_{rw} from 0.098 to 0.542. A non-monotonic relationship was found between the dispersivity and the S_{rw}. Further, analysis of the overall dispersivity of aqueous tracer in terms of the mobile-immobile-type transport equation showed the coexistence of two mass transfer mechanisms (i.e., the dispersivity of the mobile

domain and the solute exchange between the mobile and immobile domains). We introduced a dimensionless dispersivity index to quantify the relative contribution of these two mass transfer mechanisms to the overall dispersivity. However, it was found that the mass transfer of aqueous tracer in residual unsaturated porous media was controlled by the dispersion of aqueous tracer in the mobile domain at low S_{rw}, whereas it was dominated by the solute exchange between the mobile and immobile domains at high S_{rw}. Our study not only highlighted the saturation dependence of mass transfer in residual unsaturated porous media, but also emphasized the importance of the influence of saturation topology on mass transfer.

Keywords: Unsaturated Porous media; Pore scale; Mass transfer coefficient; Solute transport; Two-phase flow

1. Introduction

The aqueous tracer transport in unsaturated porous media system (i.e., at least immiscible fluids) occurs in natural processes, industrial applications and innovative tracer technologies, such as sustainable unconventional irrigation processes, enhanced oil recovery, geothermal energy development, remediation of organic contaminated groundwater, interfacial partitioning tracer test, and even cardiovascular surgeries [1-3]. Despite numerous significant advancements in solute transport in the saturated porous media system, characterizing aqueous tracer transport under the saturated porous media system was fundamentally different from that when the wetting phase (e.g., water) and the non-wetting phase (e.g., air or immiscible organic liquid) coexisted in the pore space [4, 5]. In the unsaturated porous media system, the aqueous tracer transport was significantly dependent on the complex dynamics of both immiscible two-phase flow and intricate wetting phase flow [6-8]. Therefore, understanding the mass transfer for the aqueous tracer transport in unsaturated porous media system has been more challenging than in saturated porous media system.

In recent decades, the heterogeneity of porous or fractured media has been recognized as the main reason why the hallmark of Fick's Law or traditional Fickian transport model (i.e., advection-dispersion equation or ADE) is uncapable of describing the anomalous (non-Fickian) Breakthrough curves (BTCs) [9-13]. As

typical characteristics of anomalous BTCs, the early arrival and long tails of the BTCs are ubiquitous since the heterogeneous pore space yields non-uniform flow field. The flow behavior as a background information of aqueous tracer transport was intrinsically coupled with the mass transfer of the aqueous tracer. As fundamental processes of mass transfer, the dispersion of aqueous tracer is complex because the non-uniform flow field varies in both magnitude and direction as a result of meandering through the heterogeneous pore space. The heterogeneity of the porous media caused the tortuous and spatially variable flow pathways. The corresponding flow field was consequently split into flowing and stagnant regions, referring to as mobile and immobile regions for aqueous tracer transport. In the mobile region, the mass transfer of aqueous tracer was mainly controlled by advection, while the mass transfer in the immobile region was predominantly diffusion controlled due to the poor connectivity to the main flow pathways [5, 14, 15]. The mass exchange between the mobile and immobile regions could substantially delay the transport of the aqueous tracer, associating with the tailing of the tracer BTCs. To this end, several remarkable models were developed to characterize and explain the anomalous BTCs and corresponding transport behaviors [11, 16-18], such as the continuous time random walk (CTRW)[19], the fractional advection-dispersion equation (FADE) [20], the mobile-immobile model (MIM) [21], and the multi-rate mass transfer model

(MRMT) [22]. Although, fitting anomalous BTCs to different transport models is capable of accurately estimating the transport parameters and quantify the characterization of the non-Fickian transport behaviors, application of these models in the unsaturated porous media system is limited and complex due to the variable pore space in immiscible two-phase flow condition [23-25]. Especially, even at the same hydraulic gradient, the flow field could be different depending on the saturation topology. As a result, previous studies [6, 26, 27] have indicated that the aqueous tracer transport behavior is sensitive to the saturation topology in the unsaturated porous media system.

In contrast to the saturated porous media system, the behavior of the aqueous tracer transport in the unsaturated porous media system was coupled by two fundamental fluid flow processes: (1) the mass transfer of the aqueous solute; (2) the immiscible two-phase multiphase flow. Thus, the aqueous tracer transport in unsaturated porous media system is strongly influenced by the wetting-phase saturation (e.g., water saturation) [27-29] and the spatiotemporal distribution of the two immiscible liquid phases [6]. In general, the dispersion coefficient of the aqueous tracer is an important parameter that depends on the flow velocity and water saturation. Moreover, it has been shown that the non-uniformity of the flow field with decreasing water saturation leads to a dispersion process that is non-Fickian to a larger extent [30, 31]. Raoof and Hassanizadeh [32] found that the dispersivity of

the aqueous tracer increased with decreasing water saturation, reached a maximum value and then decreased with further decreasing saturation. Recently, Hasan et al. [5] directly characterized solute transport in unsaturated porous media system by fast X-ray synchrotron microtomography and demonstrated that the dispersivity changed with water saturation. Zhuang et al. [33] studied the influence of fluid saturation and particle size on the dispersivity of solutes and found a non-monotonic relationship between the dispersivity and water saturation. These studies could be valid only for the condition where both immiscible fluids are continuous in the unsaturated porous media system. However, the law of solute transport in condition where the immiscible fluid becomes discontinuous and is immobilized by capillary forces at residual saturation has not been fully investigated.

In fact, understanding the influence of residual saturation on aqueous tracer transport is significant for many industrial applications (e.g., remediation of organic contaminated groundwater) [34, 35]. For instance, the contaminant (e.g., non-aqueous phase liquid, NAPL) could be immobilized due to capillary forces when the NAPL is at residual saturation. Consequently, the ambient flow field was changed with both the residual NAPL saturation and the spatial distribution of residual NAPL. In previous studies [36, 37], the increased longitudinal dispersivity of the aqueous tracer induced by residual NAPL was observed. Zhang et al. [38]

conducted solute transport experiments in sand columns contaminated with diesel and engine oil at different oil saturations. They also found that the dispersivity increased with increasing residual oil saturation, and further emphasized that the immobile oil trapped in the pore space could enhance the local velocity variations and increase the tortuosity of the flow paths in the aqueous phase. However, at a certain residual saturation, the spatial distribution of the residual defending phase depends on the fluid–fluid displacement processes, which are governed by the competition between viscous and capillary forces [39-43]. The competition between these two forces leads to the basic two-phase displacement patterns, such as viscous fingering, capillary fingering, and stable displacement [44]. The different two-phase displacement patterns lead to different spatial distribution of the residual defending phase. Therefore, it is necessary to characterize aqueous tracer transport through the residual two-phase zone with consideration of the two-phase displacement patterns.

The main objective of this study is to investigate the aqueous tracer transport through residual unsaturated porous media in which three phases coexist (e.g., wetting phase, non-wetting phase and solid). To this end, a pore-scale numerical simulation (PSNS) model was developed at pore scale to include both immiscible two-phase flow transport and aqueous-miscible solute transport to capture the topology of residual saturation and the tempo-spatial evolution of the aqueous

tracer in residual unsaturated porous media. Both the residual distribution pattern and the aqueous flow field in residual unsaturated porous media were analyzed. The advection-dispersion-equation (ADE), CTRW, and MIM models were inversely used to characterize the BTCs and the mass transfer mechanism of the aqueous tracer. Two different mass transfer mechanisms in terms of the MIM parameters were proposed for the overall dispersivity of the aqueous tracer. Furthermore, the dimensionless dispersivity index was introduced to quantify the relative contribution of the different mass transfer mechanisms, which provided insights into the anomalous characteristics of mass transfer of aqueous tracer in residual unsaturated porous media.

2. Methodology

2.1 Porous media geometry

The porous medium was assumed to be circular grains and the location of the grains was determined by the random procedure proposed by Dou et al. [45]. The random procedure is the general scheme to reconstruct the porous media[46]. In Step 1, we first estimated the number of grains based on the target porosity (φ'), mean radius $\bar{r}$ (L)and domain size. In Step 2, a group of radius data following a truncated lognormal distribution were generated. Second, the random number generators were used to generate the center of the grains. It should be noted that

the grains were spaced at a minimum distance to avoid overlapping. Meanwhile, we placed the grains in the domain in the order from the largest to the smallest size. This strategy is effective to save computational cost and reduce porosity. In Step 3, repeat Step 2 until the porosity reaches the target value. The porosity φ' of porous medium was calculated by:

$$\varphi' = 1 - \sum_{i=1}^{n} \frac{\pi {r_i}^2}{S} \tag{1}$$

where n is the number of grains in the domain, r_i is the radius of grain, and S is the area of domain.

359 circular grains were randomly distributed in a pore-scale domain of 41×18 mm^2, as shown in Fig. 1. The mean radius $\bar{r}$ (L) and the standard deviation of the radius distribution δ (L) were set to 0.60 mm and 0.15 mm, respectively. This means that grains radius range from 0.6-2×0.15 mm to 0.6+2×0.15 mm. The coefficient of variation (COV = $\delta/\bar{r}$) was equal to 0.25. The larger COV, the less uniform the grains radius. The porosity of the generated porous medium was set to 0.42. The randomly distributed grains and non-uniform grain size lead to a complex pore space structure. Compared to a porous medium that has the same grain radius or a medium where the grains are regularly distributed, the pore space

in our porous medium is more complex and tortuous. Therefore, the porous medium in this study can be considered as heterogeneous.

2.2 Pore-scale numerical simulation (PSNS) model description

2.2.1 Immiscible two-phase transport model: Phase Field Method (PFM)

To simulate immiscible two-phase flow transport and to obtain the residual non-wetting phase distribution in generated porous media, an immiscible two-phase transport (ITPT) model was here presented by coupling modified Navier-Stokes equation (includes a field-dependent surface tension force) with advective Cahn-Hilliard equation. For an isothermal, incompressible, and Newtonian fluid, the fluid flow in porous media is directly solved by the modified Navier-Stokes equation (Eq. (2)) and continuity equation (Eq. (3)), representing the conservation of momentum and mass for the fluid flow, respectively,

$$\rho \frac{\partial u}{\partial t} + \rho u \cdot \nabla \boldsymbol{u} = -\nabla p + \nabla \cdot [\mu(\nabla \boldsymbol{u} + \nabla \boldsymbol{u}^T)] + F_{st} \quad (2)$$

$$\nabla \cdot \boldsymbol{u} = 0 \quad (3)$$

where ρ is the density of fluid ($\mathrm{ML^{-3}}$), p is the fluid pressure ($\mathrm{ML^{-1}T^{-2}}$), $\boldsymbol{u}$ is the flow velocity of fluid ($\mathrm{LT^{-1}}$), t is the time (T), μ is the dynamic viscosity of fluid ($\mathrm{ML^{-1}T^{-1}}$), and F_{st} is the surface tension force acting at the interface between two immiscible fluids ($\mathrm{ML^{-2}T^{-2}}$).

In the absence of the description of fluid/fluid interface movement, Eqs. (2) and (3) is incapable of simulating the immiscible two-phase transport. Alternatively, to capture the fluid/fluid interface during the transport, an interface tracking method, phase field method (PFM), was used to track the interface movement and couple with Eqs. (2) and (3). The PFM is thermodynamic-based and assumes the interface between two immiscible fluids as a physically diffuse layer with thin but non-zero thickness. The phase-field parameter, ϕ, associating with a continuous variation over the thin interfacial layer but uniformity in both bulk fluids, was introduced to separate the two immiscible fluids and track the interface. For instance, the interfacial layer can be considered as the region where the ϕ varies from -1 to 1, while the two immiscible fluids can be presented by ϕ=1 and ϕ=-1, respectively. The dynamics of the ϕ can be described by a free-energy density model for an isothermal immiscible two-phase flow system [47]. The free energy is given as,

$$\mathrm{F}(\phi) = \int_{\Omega} \left[f_D(\phi) + \frac{1}{2}\lambda|\nabla\phi|^2 \right] d\Omega \tag{4}$$

where Ω represents the space occupied by the two immiscible fluids and λ is the magnitude of the mixing energy (MLT^{-2}). The terms on the right-hand side of Eq. (4), $f_D(\phi)$ and $\frac{1}{2}\lambda|\nabla\phi|^2$, account for the bulk energy and the surface energy, respectively. $f_D(\phi)$ is defined by considering a double-well potential [48],

$$f_D(\phi) = \frac{\lambda}{4\varepsilon^2}(\phi+1)^2(\phi-1)^2 \tag{5}$$

where ε represents the thickness of the interface between the two immiscible fluids (L). The surface tension coefficient, σ (MT^{-2}), can be related to both parameters λ and ε,

$$\sigma = \frac{2\sqrt{2}}{3}\frac{\lambda}{\varepsilon} \tag{6}$$

The chemical potential, $\xi(\phi)$, is introduced as [49]

$$\xi(\phi) = \frac{\delta F}{\delta \phi} = \lambda\left[-\nabla^2\phi + \frac{\phi(\phi^2-1)}{\varepsilon^2}\right] \tag{7}$$

where $\frac{\delta}{\delta\phi}$ denotes the variational differentiation of the free energy (Eq. (4)) of the interface region with respect to ϕ. By considering the mass flux as proportional to the gradient of $\xi(\phi)$, the advective Cahn-Hilliard equation is given as,

$$\frac{\partial \phi}{\partial t} + \boldsymbol{u}\cdot\nabla\phi = \nabla\cdot\left(\frac{\gamma\lambda}{\varepsilon^2}\nabla\psi\right) \tag{8}$$

$$\psi = -\nabla\cdot\varepsilon^2\nabla\phi + (\phi^2-1)\phi \tag{9}$$

where γ is the mobility parameter ($\mathrm{M}^{-1}\mathrm{L}^3\mathrm{T}$) and denotes the moving velocity of the interface under a unit driving force. γ can be considered as a function of ε,

$$\gamma = \chi\varepsilon^2 \tag{10}$$

where χ is the mobility tuning parameter. Since the χ defineds the interfacial relaxation time and determines the time scale of the Cahn-Hilliard diffusion, the

value of the χ is crucial for the numerical stability of the immiscible two-phase transport model. The value of χ must be high enough to keep the interface thickness constant and low enough not to damp the advection [50].

Recalling the surface tension force F_{st} in the modified Navier-Stokes equation (Eq. 2), the F_{st} now can be related to the phase-field parameter ϕ and given as,

$$F_{st} = \xi(\phi)\nabla\phi \tag{11}$$

Both density and viscosity in Eq. (2) are the functions of the phase-field parameter and defined as,

$$\rho = \frac{1+\phi}{2}\rho_{nw} + \frac{1-\phi}{2}\rho_{w} \tag{12}$$

$$\mu = \frac{1+\phi}{2}\mu_{nw} + \frac{1-\phi}{2}\mu_{w} \tag{13}$$

2.2.2 Pore-scale aqueous solute transport (PSAST) model

The pore-scale aqueous solute transport model was used to simulate the aqueous-miscible tracer transport in residual unsaturated porous media. For groundwater flow, the velocity is normally small (from 0.1 m/d to 10 m/d) and laminar. The aqueous flow field is solved directly using the continuity equation (Eq. (3)) and the N-S equation (Eq. (14)) under isothermal, incompressible, Newtonian, and steady-state flow conditions,

$$\rho \boldsymbol{u} \cdot \nabla \boldsymbol{u} = -\nabla p + \nabla \cdot [\mu(\nabla \boldsymbol{u} + \nabla \boldsymbol{u}^T)] \quad (14)$$

For the concentration field of the aqueous-miscible tracer, the advection-diffusion equation was used,

$$\frac{\partial c}{\partial t} = -\nabla(\boldsymbol{u}c) + D_m \nabla^2 c \qquad x \in \Omega_f \quad (15)$$

where c is the aqueous-miscible tracer concentration (ML^{-3}), D_m is the molecular diffusion coefficient ($\mathrm{L}^2\mathrm{T}^{-1}$), and the 2D velocity tensor $\boldsymbol{u}$ (LT^{-1}) is determined by the numerical solution of Eqs. (3) and (14).

3. Numerical modeling strategy and setup

In this study, the void space in porous media was initially saturated by the non-wetting phase liquid. Trichloroethylene (TCE) was assumed to be the non-wetting phase liquid and water was introduced as the wetting phase liquid. Water was injected into porous media at three injection rates to displace the TCE. In immiscible fluid-fluid displacement process, Lenormand [41] proposed the pioneered phase diagram to distinguish displacement patterns by two dimensionless numbers (e.g., capillary number *Ca* ($Ca=\mu_i v_i/\sigma$) (-) and viscosity ratio *M* ($M=\mu_i/\mu_d$) (-), where μ_i and μ_d are the viscosity of the invading and defending fluids, respectively, v_i is the characteristic velocity of the invading fluid, and σ is the interfacial tension). The *Ca* quantifies the relative magnitude of the

viscous force to the capillary force. To obtain the residual TCE distribution patterns, the displacement processes were considered. The IPTP model was first implemented with three different capillary numbers (*Ca*) ranging from $\log Ca$=-4.12 to -6.60, while the viscosity ratio (*M*) was constant and the $\log M$ was equal to 0.64. Fig. 2 showed the corresponding displacement regimes depending the previous results [51] and [41]. The left and right boundaries of the porous medium were the inlet and outlet boundaries, respectively. Water was injected along the inlet boundary at three specific flow rates (e.g., u=0.60, 0.15, and 0.05 m/s). The outlet boundary was set as zero pressure boundary condition. The non-slip boundary condition was applied to the immiscible interfaces between TCE, water and soil.

Since the residual TCE was trapped, the aqueous space for the tracer transport varied with the residual saturation of TCE. Once the residual TCE distribution was obtained via the IPTP model, the PSAST model was then employed to simulate the aqueous tracer transport in the varied aqueous pore space. The simulation flowchart was given in Fig.3 to illustrate the simulation strategy. It should be noted that the immiscible interface between TCE and water could absorb aqueous tracer due to the physical and chemical properties of tracer. However, in this study, we focused on the influence of water saturation topology on the aqueous-miscible tracer transport. The surface reaction on immiscible interface was neglected. Thus,

298 the non-reactive aqueous-miscible tracer was considered and the immiscible
299 interfaces between TCE, water and soil were assumed as a non-slip boundary for
300 the aqueous tracer transport. The no-slip boundary condition was applied at the
301 solid-liquid and liquid-liquid interfaces. There was no flux across the top and
302 bottom boundaries. For the aqueous solute transport, the pore space was initially
303 occupied by water, and there was no tracer in the aqueous pore space. The pulsed
304 tracer with concentration c_0 was injected along the inlet boundary. The step
305 function was used to simulate the pulsed injection condition. A detailed setup of
306 IPTP and PSAST models, parameters were given in the Supporting Information.
307 Two validation cases (see Supporting Information) were performed and compared
308 with the results of previous studies or theoretical value, which validate the
309 correctness of numerical models.

310 **4. Results and discussion**

311 **4.1 Residual distribution pattern in unsaturated porous media**

312 The fluid-fluid displacement patterns were determined by both *Ca* and *M*. As the
313 viscosity ratio (*M*) was constant in this study, the amount of residual TCE was
314 related to *Ca.* To obtain the different residual TCE distribution patterns, the
315 immiscible fluid-fluid displacement processes (e.g., Case I-III) at the capillary
316 numbers of $\log Ca$=-4.12, -5.50, and -6.60 were simulated by implementing the

IPTP model. As a result, we obtained four porous media with residual TCE saturation $S_{rw} = 0$, 0.098, 0.302, and 0.542. It should be mentioned that since the residual TCE as the non-wetting phase could varied the pore space of wetting phase, in this study, we focused on the residual TCE distribution pattern rather than the fluid-fluid displacement pattern during displacement processes. Fig. 4 showed the immiscible fluid-fluid displacement processes at the different *Ca*. The water, as the wetting phase, invaded into the non-wetting phase zone from the left side of the porous media domain. Due to the decreased injection rate at the inlet boundary, as expected, the breakthrough time t_{br} of the invading water increased. The t_{br} was 0.0724 s, 0.298 s, and 1.3s at logCa=-4.12, -5.50, and -6.60, respectively. The different t_{br} implied that changing the capillary numbers could affect the immiscible fluid-fluid displacement processes.

From Fig. 4, it can be seen that as capillary number decreased from logCa=-4.12 to -6.60, the displacement pattern transitions varied from compact displacement to capillary fingering. The displacement processes in Figs. 4(a)-(c) showed the typical characteristics of compact displacement. The invading water efficiently displaced the defending TCE from pore space. This is because that the pressure of the invading water sufficiently overcome the entry pressure of pore space, ever for the small pore. However, the individual TCE ganglia, as shown in Fig. 4(b), were separated from the defending TCE and were trapped in the pore throats due to the

337 snap-off process. As the capillary number decreased to logCa=-5.50, the individual
338 TCE ganglia were not only trapped in the pore throats but also formed several TCE
339 pools and significantly varied the geometry of the original pore space. Fig. 4(G)
340 showed the potential dead-end pore for the water transport due to the trapped TCE
341 ganglia. As the capillary number decreased to logCa=-6.60, a distinct change for
342 the displacement pattern marked the transition to the capillary fingering regime, as
343 shown in Figs. 4(i)-(k). It clearly showed the fingering phenomena during the
344 displacement process. The invading water prefers to advance from a large pore due
345 to the small entry pressure. The pressure of the invading water is low and
346 insufficient to displace the TCE in the small pore. Thus, even though the
347 breakthrough time t_{br} of Case III was longer than that of the Case I and Case II,
348 the TCE recovery efficiency of Case III was lower than that of the Case I and Case
349 II. Figs. 4(d), (h) and (l) showed the residual TCE distribution patterns for the Case
350 I-III. The residual TCE saturation S_{rw} was 0.098, 0.302, and 0.542 for the Case I-
351 III, respectively. This indicated that the increasing capillary number of invading
352 water could decrease the residual TCE saturation. This result agreed with the
353 previous studies [38, 42, 44, 52]. Furthermore, from Figs. 4(d), (h) and (l), it can be
354 seen that the residual TCE distribution patterns varied significantly with the
355 capillary number. For the large capillary number, the residual TCE was distributed
356 in small throat among pores, while in displacement morphologies of capillary

finger, the invading water paths formed several fingers due to the heterogeneity of porous media. It should be noted that when the main invading water finger breaks through the outlet, the pressure of the invading water decreases dramatically. Thus, other invading water fingers fail to break through the outlet and forms a typical dead-end flow pathway, as shown in Fig. 4(K).

4.2 Aqueous flow field in residual unsaturated porous media

Once the defending TCE was trapped in the pore space at the residual saturation, the defending TCE become the residual TCE which was discontinuous and immobilized due to the capillary force. As the non-wetting phase, the residual TCE varies the pore structure and the pore space where provides the potential space for the aqueous flow and the aqueous solute transport. We here analyzed the influence of residual TCE distribution on the aqueous flow field by considering the residual TCE as the invalid domain for the aqueous flow. The detail of solving the aqueous flow field and setting the boundary condition can be found in the Supporting Information.

From Fig. 5, it can be seen that the aqueous flow pathways were significantly changed due to the residual TCE. Comparing Figs. 5 (a) with 4 (b), the main flow pathway in the original porous media was almost the same as that in Case I. The corresponding mean flow velocities were 6.30×10^{-4} m/s and 6.65×10^{-4} m/s for the

original porous media and Case I, respectively. There is a slight increase (about 5.6%) in the mean flow velocity. This is because that for Case I (see Fig. 5(b)), the residual TCE was trapped in the small pore throat between the grains and was mainly located near the upper and lower boundaries, where the flow velocity was originally low. As the capillary number decreased, the displacement pattern marked the transition to the capillary fingering regime, resulting not only in a dramatical increase in S_{rw} but also in a significant variation in the residual TCE distribution. From Figs. 5 (c) and (d), it can be seen that the geometry of the main flow pathway was significantly changed by the residual TCE. The corresponding mean flow velocities were 4.61×10^{-4} m/s and 4.59×10^{-4} m/s in Case II and Case III, respectively. Compared with the mean flow velocity in the original porous media, the values of mean flow velocity for Case II and Case III decreased by 26.8% and 27.1%, respectively. In particular, the displacement pattern with a typical characteristic of capillary fingering leads to more residual TCE in Case III than in Case I and Case II. In Case III, there are two different preferential flow pathways through the porous medium in Case III. Several dead-end pathways caused both the drastic decrease of the mean flow velocity and the significant variation of the aqueous flow field.

On the one hand, the residual TCE leads to a variation of the mean flow velocity in the aqueous flow field, and on the other hand, it could enhance the heterogeneity of

the aqueous flow field due to its different distributions. To quantitatively evaluate the influence of the residual TCE distribution on the heterogeneity of the aqueous flow field, we estimated the probability density functions (PDFs) of flow velocity [53, 54] and introduced the coefficient of velocity variation (*CV*) as a global measure of the velocity spatial variability [14]. For incompressible flow, the coefficient of velocity variation was defined as follows,

$$CV_{\boldsymbol{u}} = \frac{\sigma_{\boldsymbol{u}}}{\overline{\boldsymbol{u}}} = \frac{\sqrt{\int_V (\boldsymbol{u}-\overline{\boldsymbol{u}})^2 \frac{dV}{V}}}{\int_V \overline{\boldsymbol{u}} \frac{dV}{V}} \tag{16}$$

where the $\sigma_{\boldsymbol{u}}$ is the standard variance of the flow velocity, $\overline{\boldsymbol{u}}$ is the mean flow velocity, and V is the volume of the pore space occupied by aqueous fluid.

From Fig. 6, it can be seen that in both the original porous media and Case I-III, the PDFs of the longitudinal flow velocity (u_x) were skewed towards positive values with an approximately stretched exponential shape. For the PDFs of u_x (see Fig. 6(a)), there were small negative velocities in all cases, indicating the presence of backflow. It was found that with increasing residual TCE saturation and the change from compact displacement patterns to capillary fingering, the tailing of the PDFs for both u_x and $\boldsymbol{u}$ decreased significantly. This indicated that with increasing residual TCE saturation, the range of flow velocity distribution in the aqueous flow field decreased, which was associated with the decreased high flow velocity.

Moreover, the $\sigma^2_{(\boldsymbol{u})}$ decreased slightly with increasing residual TCE saturation, whereas the $\sigma^2_{ln(\boldsymbol{u})}$ increased dramatically. This reflected the formation of both the preferential flow pathways with high velocities and the stagnant flow zone with low velocities. It was found that the $CV_{\boldsymbol{u}}$ increased with increasing residual TCE saturation, indicating that the velocity spatial variability in the Case I-III was much stronger than that in the original porous media. Thus, with increasing residual TCE saturation, not only the tailing of the PDFs for both u_x and $\boldsymbol{u}$ decreased significantly, but also the velocity spatial variability in the aqueous flow field was enhanced.

4.3 Behaviors of aqueous tracer transport and BTCs

Fig. 7 showed the aqueous tracer transport in both the original porous media and Case I-III. Due to the significant change of the pore structure caused by the residual TCE, the spatial evolution of the aqueous tracer in Case I-III was significantly different from that in the original aqueous flow field. As the residual TCE saturation increased, the area of the potential zone for aqueous tracer transport decreased. For the capillary fingering displacement (e.g., Case III), the aqueous tracer pathways formed several fingers and were independent of the pore structure in original porous media. Several dead-end pathways for aqueous tracer transport were observed in both Case II and Case III. The aqueous tracer transport into these dead-end pathways is limited due to the slow diffusion-dominant

process. It should be mentioned that the *Pe* were greater than 200 in all cases (see Table 1), indicating that the aqueous tracer transport was advection-dominant. However, the aqueous tracer transport in several dead-end pathways was diffusion-dominant due to the extremely low flow velocity. As shown in Figs. 7(l) and (p), once the aqueous tracer was transported into the dead-end pathways, a certain amount of aqueous tracer was entrained and the mass exchange processes between the dead-end pathways and the preferential pathways become rate-limited. Consequently, the trapped aqueous tracer in dead-end pathways could lead to anomalous transport behaviors (e.g., long tails of the BTCs). In addition, due to the enhanced velocity spatial variability, the aqueous tracer in the preferential flow pathways was not only transported faster but also had a higher concentration in Case II and Case III than in the original porous media and Case I.

As a cumulative consequence of aqueous tracer transport through the unsaturated porous media system, the BTCs reflect the temporal evolution of the aqueous tracer. In Fig. 8, all BTCs exhibited typical characteristics of anomalous aqueous tracer transport (e.g., the early arrival and long tails of the BTCs), although the aqueous tracer was transported in the original porous media where no residual TCE changed the pore structure. This indicates that not only the residual TCE but also the heterogeneity of the original porous media can lead to the anomalous aqueous tracer transport. As can be seen in Fig. 8, the early arrival and long tails of the

454 BTCs were the same in the original porous media and Case I. This is because that
455 the aqueous flow field was almost the same, since the compact displacement
456 pattern in Case I efficiently displaced the defending TCE from the pore space and
457 the variation of pore structure was trivial. As the capillary number decreased, the
458 immiscible fluid-fluid displacement pattern marked the transition to the capillary
459 fingering regime and the residual TCE saturation increased, associating the
460 significantly varied pore structure. Thus, the velocity spatial variability in the
461 aqueous flow field was enhanced. Consequently, the early arrival and long tails of
462 the BTCs were pronounced in Case II and Case III than in the original porous
463 media and Case I. Although the residual TCE significantly varied the pore
464 structure in Case II and Case III, the early arrival of the BTCs was the same while
465 the long tails of the BTCs was different in Case II and Case III. This indicates that
466 the residual TCE in Case II and Case III has little influence on the mean flow
467 velocity while has significant influence on the mass transfer between the mobile
468 and immobile domains.

469 To evaluate quantitatively the anomalous transport characteristics, we used both
470 traditional ADE model and CTRW model inversely to fit the BTCs. Detailed
471 information on the goodness-of-fitting of both ADE model and CTRW model can
472 be found in the Supporting Information. Table 2 showed the goodness-of-fit results
473 of the ADE and CTRW models.

As listed in Table 2, the coefficient of determination R^2 is about 1.0 and the global error E_i was low, indicating the ability to characterize aqueous tracer transport by using both ADE and CTRW model. As a key parameter in the CTRW model, β_{CTRW} characterizes the dispersion regime. According to the previous study [55], $0 < \beta_{CTRW} < 1$ indicated a highly anomalous transport; $1 < \beta_{CTRW} < 2$ was associated with a moderately anomalous transport; $\beta_{CTRW} > 2$ corresponded to the Fickian transport. Table 2 showed that all β_{CTRW} were close to 2.0, indicating that all aqueous tracer transports in this study are moderately anomalous. The mean flow velocities $\overline{u_{ADE}}$ and $\overline{u_{CTRW}}$ were dependent on the residual TCE distribution and showed the same trend as the pore structure varied by the residual TCE. The dispersivities were determined as $\alpha_{L,ADE}(= D_{ADE}/\overline{u_{ADE}})$ and $\alpha_{L,CTRW} = (D_{CTRW}/\overline{u_{CTRW}})$ in ADE and CTRW models, respectively. In Table 2, the results indicated a non-monotonic relationship between the dispersivity and the S_w in both ADE and CTRW models. Due to the high S_w and almost unchanged pore structure, the dispersivity was slightly lower in Case II than in the original porous media. This suggested that the residual TCE resulting from the compact fluid-fluid displacement process had a small influence on the aqueous tracer transport. It was found that the dispersivity was enhanced in Case II when the pore structure was significantly changed and the S_w was decreased due to the residual TCE. However, the dispersivity showed a slight decrease in Case III where the pore structure was

494 significantly changed and the velocity spatial variability of the aqueous flow field
495 was enhanced. It should be noted that since both ADE and CTRW models were
496 assumed to be one-dimensional, the dispersivity by both ADE and CTRW models
497 could be expected to be the averaged dispersivity over the whole domain.
498 Therefore, it was insufficient to characterize the mass transfer of the aqueous tracer
499 transport only by the dispersivity. In other words, our results indicated that the
500 dispersivity of aqueous tracer was dependent on not only the S_w but also the
501 distribution of the residual TCE that related to the immiscible fluid-fluid
502 displacement regime.

503 **4.4 Mass transfer**

504 Since the residual TCE varies the pore structure and space of the wetting phase
505 where provides the potential space for the aqueous flow field and the aqueous
506 tracer transport, the corresponding flow field was consequently split into flowing
507 and stagnant regions, referring to as mobile and immobile regions for aqueous
508 tracer transport. The solute exchange between the mobile and immobile regions
509 could substantially delay the transport of the aqueous tracer, associating with the
510 tailing of the tracer BTCs. The tailing of the tracer BTCs is also related to the
511 reaction at the solid-fluid interface, which can be assessed by the Sherwood
512 number[56]. In this study, the tracer was assumed to be non-reactive. Therefore,
513 we focus on the solute exchange between the mobile and immobile regions. To

514 quantify this mechanism, we proposed to estimate the mass transfer for aqueous
515 tracer transport by MIM model. The MIM model is a time nonlocal transport
516 model, which describes the diffusion-driven mass exchange between the mobile
517 and immobile domains. The single mass-transfer rate MIM model could capture
518 the non-Fickian solute transport caused by the diffusion-limited transport of solutes
519 in immobile zones. The MIM transport equation is given by [21]

520 $$\frac{\partial C_m}{\partial t} + \left(\frac{S_{sw}}{S_w - S_{sw}}\right)\frac{\partial C_{im}}{\partial t} = -\overline{u_m}\frac{\partial C_m}{\partial x} + D_{f,mim}\frac{\partial^2 C_m}{\partial x^2} \quad (17)$$

521 where C_m and C_{im} represent the concentration of the aqueous tracer in the mobile
522 (flowing) and immobile (stagnant) domains in the wetting phase respectively;
523 $D_{f,mim}$ is the fitted dispersion coefficient and $\overline{u_m}$ is the effective flow velocity in
524 mobile domain for the wetting phase; S_w is the saturation of wetting phase, which
525 is equal to the sum of the stagnant saturation S_{sw} and the flowing saturation S_{fw} in
526 the wetting phase. A partitioning coefficient $\beta = (S_w - S_{sw})/S_w = S_{fw}/S_w$ was
527 introduced as the mobile domain fraction in the wetting phase. Thus, the $\overline{u_m}$ in Eq.
528 (17) is related to the mean flow velocity of the wetting phase ($\overline{u_{MIM}}$) by
529 $\overline{u_m} = \overline{u_{MIM}}/\beta$. The dispersivity $\alpha_{L,mim}$ $(= D_{f,mim}/\overline{u_m})$ in MIM model was
530 determined for all cases. The solute exchange between the mobile and immobile
531 domains was described by a nonequilibrium mass transfer model,

$$S_{sw}\frac{\partial C_{im}}{\partial t} = \alpha(C_m - C_{im}) \quad (18)$$

where α is the mass transfer coefficient between the mobile and immobile domains. For MIM model, the best-fit parameters $D_{f,mim}$, α, and β were estimated. The initial estimate of the parameters has a great influence on the accuracy of the inverse parameters, and an accurate initial estimation could improve the convergence to a minimum error. The initial values of $\overline{u_m}$ and $D_{f,mim}$ were set to the counterpart values calculated by the ADE model. The STANMOD V2.08 based on CXTFIT code[57] was employed for the inversion of MIM model.

Table 3 listed the parameters estimated from MIM model. As shown in Table 3, both the R^2 close to 1.0 and the low E_i ensured the reliability and accuracy of the inversion of MIM model. As listed in Table 3, β showed a non-monotonic decrease with decreasing S_w. Note that our result of β reflects two aspects. First, the maximum β was observed at $S_w = 1.0$ (e.g., saturated conditions), which is consistent with the previous study [58]. Second, the low β was observed at $S_w = 0.698$ in Case II rather than at lower saturation (e.g., $S_w = 0.458$ in Case III). This implies that the larger domain fraction in the wetting phase become immobile for aqueous tracer transport at $S_w = 0.458$ rather than at $S_w = 0.698$. This could be attributed to the discontinuous residual TCE formed by the different patterns of the immiscible fluid-fluid displacement. More especially, the residual distribution of

TCE at $S_w = 0.458$ resulted from the transition of the displacement pattern from the compact displacement to the capillary fingering regime. Unlike compact displacement and capillary fingering displacement, there were remarkable dead-end pathways with the stagnant flow velocity in this transition displacement, which is consequently unfavorable for advection-dominant transport of the aqueous tracer. Therefore, the β in residual unsaturated porous media was affected by not only the S_w but also the residual saturation topology.

In Table 3, the maximum $\alpha_{L,mim}$ was observed at $S_w = 0.698$ in Case II and the relationship between $\alpha_{L,mim}$ and S_w showed a non-monotonic relation, similar as for both ADE and CTRW models. It should be mentioned that the $\alpha_{L,mim}$ was significantly smaller than both the $\alpha_{L,ADE}$ and the $\alpha_{L,CTRW}$, since the $\alpha_{L,mim}$ accounted only for the dispersivity of the mobile domain in the wetting phase. According to the dispersion regime of MIM model, an overall dispersivity includes both the dispersivity of the mobile domain and the influence of solute exchange between the mobile and immobile domains. Thus, the overall dispersivity α_{MIM} in terms of the MIM parameters can be defined by [59]

$$\alpha_{MIM} = \alpha_{L,mim} + \frac{S_{fw}^2 S_{sw} \overline{u_m}}{\alpha S_w^2} \tag{19}$$

We introduced $\alpha_{L,ms}$ to represent the contribution of the solute exchange between the mobile and immobile domains to the overall dispersivity α_{MIM}.

$$\alpha_{L,ms} = \frac{S_{fw}^2 S_{sw} \overline{u_m}}{\alpha S_w^2} \quad (20)$$

The dispersivities from the MIM and ADE models as functions of water saturation were shown in Fig. 9. The $\alpha_{L,ADE}$ from the ADE model was always smaller than the overall dispersivity α_{MIM} from the MIM model over all S_w, which is consistent with previous studies [33, 59]. This could be due to the inherently limited capability of ADE model for characterizing the anomalous BTCs. On the other hand, this is reasonable to characterize the overall dispersivity into the two mass transfer mechanisms (e.g., dispersion in mobile domain and solute exchange between immobile and mobile domain). As a result, the α_{MIM} as the overall dispersivity was always larger than both the $\alpha_{L,ms}$ and the $\alpha_{L,mim}$ over all S_w. Moreover, the non-zero of the $\alpha_{L,ms}$ and the $\alpha_{L,mim}$ confirmed that the coexistence of these two mass transfer mechanisms over all S_w.

It should be mentioned that the relative contribution of these two mass transfer mechanisms to the overall dispersivity is of great importance for understanding aqueous tracer transport behavior. Therefore, to evaluate the relative contribution between $\alpha_{L,ms}$ and $\alpha_{L,mim}$ in the dispersion regime of MIM model, the ,3

$$\epsilon_d = \frac{\alpha_{L,ms}}{\alpha_{L,mim}} \quad (21)$$

587 ϵ_d >1 means that the overall dispersivity is dominated by the solute exchange
588 between the mobile and immobile domains, whereas ϵ_d <1 indicates that the
589 overall dispersivity is controlled by the dispersion of aqueous tracer in the mobile
590 domain. As shown in Fig. 9, the ϵ_d as a function of S_w showed a non-monotonic
591 relationship, since the similar relationship was observed between α_{MIM} and S_w.
592 The value of the ϵ_d was 0.56, 0.49, 5.54, and 1.87 at S_w=1.0, 0.902, 0.698, and
593 0.458, respectively, indicating that the mass transfer of aqueous at high water
594 saturation conditions (e.g., S_w=1.0 and 0.902) was controlled by the dispersion of
595 aqueous tracer in the mobile domain, while at low water saturation conditions (e.g.,
596 S_w=0.698 and 0.458) it was dominated by solute exchange between the mobile and
597 immobile domains. This suggested that the mass transfer mechanism of aqueous
598 tracer varied with S_w. Interestingly, the mass transfer coefficient between the
599 mobile and immobile domains (see the α in Table 3) was found to have an overall
600 decreasing trend at ϵ_d >1. Note that $1/\alpha$ represents the time scale for solute
601 exchange between the mobile and immobile domains. $1/\alpha$ was three times larger
602 under water-saturated conditions than under conditions of low water saturation
603 conditions. This means that the exchange time was longer at low S_w, which is
604 related to slower solute mixing. Thus, if mass transfer of the aqueous tracer was
605 dominated by solute exchange between the mobile and immobile domains at low
606 S_w, the long exchange time will cause aqueous tracer transport to be retained and

607 mass transfer to be delayed. In addition, the proposed ϵ_d would provide insights
608 into the anomalous characteristics of mass transfer of aqueous tracer in residual
609 unsaturated porous media. Recall the anomalous characteristics of BTCs in Fig. 7:
610 the dominant solute exchange between the mobile and immobile domains caused
611 the remarkable long tails of BTCs at $\epsilon_d > 1$, while the early arrival of BTCs was
612 observed at $\epsilon_d < 1$, where dispersion in the mobile domain controls the mass
613 transfer of the aqueous tracer.

614 **5. Summary and conclusion**

615 In this study, the miscible-aqueous tracer transport through residual unsaturated
616 porous media in which three phases coexist was investigated. The pore-scale
617 numerical simulation was implemented to simulate the immiscible two-phase
618 transport and the pore-scale aqueous solute transport for obtaining the residual
619 distribution pattern and the aqueous flow field in residual unsaturated porous
620 media. Three different topologies of residual saturation were determined at S_{rw}=
621 0.098, 0.302, and 0.542, as the immiscible fluid-fluid displacement pattern varied
622 from compact displacement to capillary fingering. The mass transfer of aqueous
623 tracer in residual unsaturated porous media was inversely characterized by ADE,
624 CTRW, and MIM models. Two different mass transfer mechanisms in terms of the
625 MIM parameters were proposed for the overall dispersivity of the aqueous tracer.
626 The main findings of this study can be summarized by:

627 (1) Analysis of aqueous flow field in different topologies of the residual
628 saturation showed that the topology of residual saturation has a significant
629 influence on not only the PDFs but also velocity spatial variability of the aqueous
630 flow field, associating with the velocity spatial variability was enhanced with
631 increasing S_{rw}. Both ADE and CTRW model confirmed the typical characteristics
632 of anomalous aqueous tracer transport (i.e., early arrivals and long tails) in BTCs
633 in a range of S_{rw} from 0.098 to 0.542. Due to the enhanced velocity spatial
634 variability, the aqueous tracer was not only transported faster in the preferential
635 flow pathways, but also had a higher concentration at high S_{rw} than at low S_{rw}.

636 (2) A non-monotonic relationship was found between the dispersivity and the
637 S_{rw}, indicating the dependence of dispersivity on S_{rw}. The results showed the
638 coexistence of these two mass transfer mechanisms over all S_{rw} (e.g., the
639 dispersion in the mobile domain and the solute exchange between the immobile
640 and mobile domains). The dimensionless dispersivity index ϵ_d was introduced to
641 quantify the relative contribution of these two mass transfer mechanisms to the
642 overall dispersivity. The maximum of ϵ_d was 5.54 and was observed at S_{rw}=0.302.
643 It was found that the overall mass transfer at low S_{rw} was dominated by the
644 dispersion of aqueous tracer in the mobile domain, whereas at high S_{rw}, the solute
645 exchange between the mobile and immobile domains was dominant.

(3) The time scale ($1/\alpha$) for solute exchange between the mobile and immobile domains was three times larger under water-saturated conditions than under high S_{rw} conditions, with the resulting exchange time being longer. The maximum of the mobile domain fraction β in the wetting phase was observed under water-saturated conditions, however, the β showed a non-monotonic decrease with increasing S_{rw}. It was found that the transition displacement pattern from the compact displacement to the capillary fingering regime could lead to remarkable dead-end pathways with the stagnant flow velocity, resulting from the low β.

Overall, our study not only confirmed the saturation dependence of mass transfer in residual unsaturated porous media, but also emphasized the importance of considering the influence of saturation topology on mass transfer. The same value of S_{rw} may have a completely different saturation topology due to the different immiscible displacement regimes. Under these circumstances, the mass transfer dependence on S_{rw} could be ambiguous because the relative contribution of the different mass transfer mechanisms was found to be sensitive to the residual saturation topology. Althoughh the numerical modeling strategy in this study provides a better basis for considering the transport of both immiscible two-phase flow and aqueous-miscible solute, further work is clearly needed to theoretically

665 establish the relationship between the immiscible displacement regimes and the
666 mass transfer of miscible-aqueous tracer.

667

Declaration of Competing Interest

The authors declare that they have no known competing financial interests or personal relationships that could have appeared to influence the work reported in this paper.

Author Contributions

Zhi Dou: Conceptualization, Methodology, Investigation, Writing - original draft, Writing - review & editing, Supervision, Project administration, Funding acquisition. **Xueyi Zhang:** Methodology, Investigation, Visualization, Writing - original draft, Writing - review & editing. **Chao Zhuang:** Methodology, Visualization, Writing - original draft, Writing - review & editing. **Yun Yang:** Methodology, Writing - original draft, Writing - review & editing. **Jinguo Wang:** Writing - original draft, Writing - review & editing. **Zhifang Zhou:** Writing - original draft, Writing - review & editing.

Acknowledgment

The study is financially supported by the National Key Research and Development Program of China (No. 2019YFC1804303) and the National Natural Science Foundation of China (Grant No. 41877171).

Reference

[1] R. Masri, C. Puelz, B. Riviere, A reduced model for solute transport in compliant blood vessels with arbitrary axial velocity profile, International Journal of Heat and Mass Transfer, 176 (2021) 121379.
[2] H. Zhong, A. El Ouni, D. Lin, B. Wang, M.L. Brusseau, The two-phase flow IPTT method for measurement of nonwetting-wetting liquid interfacial areas at higher nonwetting saturations in natural porous media, Water Resources Research, 52(7) (2016) 5506-5515.
[3] Y. Hu, A. Patmonoaji, H. Xu, K. Kaito, S. Matsushita, T. Suekane, Pore-scale investigation on nonaqueous phase liquid dissolution and mass transfer in 2D and 3D porous media, International Journal of Heat and Mass Transfer, 169 (2021) 120901.
[4] N.K. Karadimitriou, V. Joekar-Niasar, O.G. Brizuela, Hydro-dynamic Solute Transport under Two-Phase Flow Conditions, Scientific Reports, 7(1) (2017) 6624.
[5] S. Hasan, V. Niasar, N.K. Karadimitriou, J.R.A. Godinho, N.T. Vo, S. An, A. Rabbani, H. Steeb, Direct characterization of solute transport in unsaturated porous media using fast X-ray synchrotron microtomography, Proceedings of the National Academy of Sciences, 117(38) (2020) 23443.
[6] N.K. Karadimitriou, V. Joekar-Niasar, M. Babaei, C.A. Shore, Critical Role of the Immobile Zone in Non-Fickian Two-Phase Transport: A New Paradigm, Environmental Science & Technology, 50(8) (2016) 4384-4392.
[7] V. Joekar-Niasar, B. Ataie-Ashtiani, Assessment of nitrate contamination in unsaturated zone of urban areas: The case study of Tehran, Iran, Environmental Geology, 57(8) (2009) 1785-1798.
[8] W. Hu, N. Huang, X. Zhang, Impact of saturation on mass transfer rate between mobile and immobile waters in solute transport within aggregated soils, Journal of Hydrology, 519 (2014) 3557-3565.
[9] M. Dentz, T. Le Borgne, A. Englert, B. Bijeljic, Mixing, spreading and reaction in heterogeneous media: A brief review, Journal of Contaminant Hydrology, 120–121 (2011) 1-17.
[10] Z. Dou, Z. Chen, Z. Zhou, J. Wang, Y. Huang, Influence of eddies on conservative solute transport through a 2D single self-affine fracture, International Journal of Heat and Mass Transfer, 121 (2018) 597-606.
[11] Z. Dou, B. Sleep, H. Zhan, Z. Zhou, J. Wang, Multiscale roughness influence on conservative solute transport in self-affine fractures, International Journal of Heat and Mass Transfer, 133 (2019) 606-618.
[12] Y. Jin, X. Li, M. Zhao, X. Liu, H. Li, A mathematical model of fluid flow in tight porous media based on fractal assumptions, International Journal of Heat and Mass Transfer, 108, Part A (2017) 1078-1088.
[13] L. Wang, M.B. Cardenas, Transition from non-Fickian to Fickian longitudinal transport through 3-D rough fractures: Scale-(in)sensitivity and roughness dependence, Journal of Contaminant Hydrology, 198 (2017) 1-10.
[14] M. Rolle, P.K. Kitanidis, Effects of compound-specific dilution on transient transport and solute breakthrough: A pore-scale analysis, Advances in Water Resources, 71 (2014) 186-199.
[15] W.A. Illman, Hydraulic tomography offers improved imaging of heterogeneity in fractured rocks, Groundwater, 52(5) (2014) 659-684.
[16] G. Gao, H. Zhan, S. Feng, G. Huang, X. Mao, Comparison of alternative models for simulating anomalous solute transport in a large heterogeneous soil column, Journal of Hydrology, 377(3) (2009) 391-404.
[17] S.P. Neuman, D.M. Tartakovsky, Perspective on theories of non-Fickian transport in heterogeneous media, Advances in Water Resources, 32(5) (2009) 670-680.
[18] O. Nikan, J.A.T. Machado, A. Golbabai, T. Nikazad, Numerical approach for modeling fractal mobile/immobile transport model in porous and fractured media, International Communications in Heat and Mass Transfer, 111 (2020) 104443.

[19] B. Berkowitz, A. Cortis, M. Dentz, H. Scher, Modeling non‐Fickian transport in geological formations as a continuous time random walk, Reviews of Geophysics, 44(2) (2006).
[20] D.A. Benson, The fractional advection-dispersion equation: Development and application, University of Nevada, Reno, 1998.
[21] M.T. Van Genuchten, P. Wierenga, Mass transfer studies in sorbing porous media I. Analytical solutions, Soil Science Society of America Journal, 40(4) (1976) 473-480.
[22] R. Haggerty, S.M. Gorelick, Multiple-Rate Mass Transfer for Modeling Diffusion and Surface Reactions in Media with Pore-Scale Heterogeneity, Water Resources Research, 31(10) (1995) 2383-2400.
[23] M. Boon, B. Bijeljic, S. Krevor, Observations of the impact of rock heterogeneity on solute spreading and mixing, Water Resources Research, 53(6) (2017) 4624-4642.
[24] B. Bijeljic, A. Raeini, P. Mostaghimi, M.J. Blunt, Predictions of non-Fickian solute transport in different classes of porous media using direct simulation on pore-scale images, Physical Review E, 87(1) (2013) 013011.
[25] F. Ahmad, A. Rahimi, E. Tsotsas, M. Prat, A. Kharaghani, From micro-scale to macro-scale modeling of solute transport in drying capillary porous media, International Journal of Heat and Mass Transfer, 165 (2021) 120722.
[26] P. De Gennes, Hydrodynamic dispersion in unsaturated porous media, Journal of Fluid Mechanics, 136 (1983) 189-200.
[27] K.A.M.C.A. Ramsburg, Influence of Nonwetting Phase Saturation on Dispersivity in Laboratory-Scale Sandy Porous Media, Environmental Engineering Science, 35(10) (2018) 1062-1074.
[28] S. Hasan, V. Joekar-Niasar, N.K. Karadimitriou, M. Sahimi, Saturation Dependence of Non-Fickian Transport in Porous Media, Water Resources Research, 55(2) (2019) 1153-1166.
[29] J. Jiménez-Martínez, T. Le Borgne, H. Tabuteau, Y. Méheust, Impact of saturation on dispersion and mixing in porous media: Photobleaching pulse injection experiments and shear-enhanced mixing model, Water Resources Research, 53(2) (2017) 1457-1472.
[30] M. Bromly, C. Hinz, Non‐Fickian transport in homogeneous unsaturated repacked sand, Water Resources Research, 40(7) (2004).
[31] J. Jiménez‐Martínez, P.D. Anna, H. Tabuteau, R. Turuban, T.L. Borgne, Y. Méheust, Pore‐scale mechanisms for the enhancement of mixing in unsaturated porous media and implications for chemical reactions, Geophysical Research Letters, 42(13) (2015) 5316-5324.
[32] A. Raoof, S. Hassanizadeh, Saturation‐dependent solute dispersivity in porous media: pore‐scale processes, Water Resources Research, 49(4) (2013) 1943-1951.
[33] L. Zhuang, A. Raoof, M.G. Mahmoodlu, S. Biekart, R. de Witte, L. Badi, M.T. van Genuchten, K. Lin, Unsaturated flow effects on solute transport in porous media, Journal of Hydrology, 598 (2021) 126301.
[34] M. Aminnaji, A. Rabbani, V. J. Niasar, M. Babaei, Effects of Pore-Scale Heterogeneity on Macroscopic NAPL Dissolution Efficiency: A Two-Scale Numerical Simulation Study, Water Resources Research, 55(11) (2019) 8779-8799.
[35] H.I. Essaid, B.A. Bekins, I.M. Cozzarelli, Organic contaminant transport and fate in the subsurface: Evolution of knowledge and understanding, Water Resources Research, 51(7) (2015) 4861-4902.
[36] K.D. Pennell, M. Jin, L.M. Abriola, G.A. Pope, Surfactant enhanced remediation of soil columns contaminated by residual tetrachloroethylene, Journal of Contaminant Hydrology, 16(1) (1994) 35-53.
[37] B. Rogers, B.E. Logan, Bacterial transport in NAPL-contaminated porous media, Journal of environmental engineering, 126(7) (2000) 657-666.
[38] J. Zhang, X. Zheng, L. Chen, Y. Sun, Effect of residual oil saturation on hydrodynamic properties of porous media, Journal of hydrology, 515 (2014) 281-291.
[39] B. Zhao, C.W. MacMinn, R. Juanes, Wettability control on multiphase flow in patterned microfluidics, Proceedings of the National Academy of Sciences, 113(37) (2016) 10251-10256.

[40] R. Hu, J. Wan, Y. Kim, T.K. Tokunaga, Wettability effects on supercritical CO2–brine immiscible displacement during drainage: Pore-scale observation and 3D simulation, International Journal of Greenhouse Gas Control, 60(Supplement C) (2017) 129-139.
[41] R. Lenormand, E. Touboul, C. Zarcone, Numerical models and experiments on immiscible displacements in porous media, Journal of fluid mechanics, 189(1) (1988) 165-187.
[42] Y.-F. Chen, D.-S. Wu, S. Fang, R. Hu, Experimental study on two-phase flow in rough fracture: Phase diagram and localized flow channel, International Journal of Heat and Mass Transfer, 122 (2018) 1298-1307.
[43] Z. Dou, Z. Zhou, B. Sleep, Influence of wettability on interfacial area during immiscible liquid invasion into a 3D self-affine rough fracture: Lattice Boltzmann simulations, Advances in water resources, 61 (2013) 1-11.
[44] Y.F. Chen, S. Fang, D.S. Wu, R. Hu, Visualizing and quantifying the crossover from capillary fingering to viscous fingering in a rough fracture, Water Resources Research, 53(9) (2017) 7756-7772.
[45] Z. Dou, X. Zhang, Z. Chen, Y. Yang, C. Zhuang, C. Wang, Effects of Cemented Porous Media on Temporal Mixing Behavior of Conservative Solute Transport, Water, 11(6) (2019) 1204.
[46] L. Chen, R. Zhang, T. Min, Q. Kang, W. Tao, Pore-scale study of effects of macroscopic pores and their distributions on reactive transport in hierarchical porous media, Chemical Engineering Journal, 349 (2018) 428-437.
[47] W. Villanueva, G. Amberg, Some generic capillary-driven flows, International Journal of Multiphase Flow, 32(9) (2006) 1072-1086.
[48] V.E. Badalassi, H.D. Ceniceros, S. Banerjee, Computation of multiphase systems with phase field models, Journal of Computational Physics, 190(2) (2003) 371-397.
[49] P. Yue, J.J. Feng, C. Liu, J.I.E. Shen, A diffuse-interface method for simulating two-phase flows of complex fluids, Journal of Fluid Mechanics, 515 (2004) 293-317.
[50] D. Jacqmin, Calculation of Two-Phase Navier–Stokes Flows Using Phase-Field Modeling, Journal of Computational Physics, 155(1) (1999) 96-127.
[51] C. Zhang, M. Oostrom, T.W. Wietsma, J.W. Grate, M.G. Warner, Influence of viscous and capillary forces on immiscible fluid displacement: Pore-scale experimental study in a water-wet micromodel demonstrating viscous and capillary fingering, Energy & Fuels, 25(8) (2011) 3493-3505.
[52] G. Zhu, J. Yao, A. Li, H. Sun, L. Zhang, Pore-Scale Investigation of Carbon Dioxide-Enhanced Oil Recovery, Energy & Fuels, 31(5) (2017) 5324-5332.
[53] M. Dentz, M. Icardi, J.J. Hidalgo, Mechanisms of dispersion in a porous medium, Journal of Fluid Mechanics, 841 (2018) 851-882.
[54] M. Carrel, V.L. Morales, M. Dentz, N. Derlon, E. Morgenroth, M. Holzner, Pore-Scale Hydrodynamics in a Progressively Bioclogged Three-Dimensional Porous Medium: 3-D Particle Tracking Experiments and Stochastic Transport Modeling, Water Resour Res, 54(3) (2018) 2183-2198.
[55] A. Cortis, B. Berkowitz, Anomalous Transport in “Classical” Soil and Sand Columns, Soil Science Society of America Journal, 68(5) (2004) 1539-1548.
[56] A. Xu, T.S. Zhao, L. Shi, J.B. Xu, Lattice Boltzmann Simulation of Mass Transfer Coefficients for Chemically Reactive Flows in Porous Media, Journal of Heat Transfer, 140(5) (2018).
[57] N. Toride, F. Leij, M.T. Van Genuchten, The CXTFIT code for estimating transport parameters from laboratory or filed tracer experiments, US Salinity Laboratory Riverside, CA, 1995.
[58] J. Griffioen, D. Barry, J.Y. Parlange, Interpretation of two‐region model parameters, Water Resources Research, 34(3) (1998) 373-384.
[59] N. Toride, M. Inoue, F.J. Leij, Hydrodynamic dispersion in an unsaturated dune sand, Soil Science Society of America Journal, 67(3) (2003) 703-712.

List of Figure Captions

Fig. 1 The generated porous medium and the distribution of grain diameter

Fig. 2 logCa - log$M$ phase diagram of the fluid-fluid displacement morphologies. The viscous fingering, capillary fingering, and stable displacement zones bounded by the black dash-dot line and the grey zone are obtained by [51] and [41], respectively.

Fig. 3 Flowchart of simulation

Fig. 4 Immiscible fluid-fluid displacement processes and residual patterns at logCa=-4.12 (Case I), logCa=-5.50 (Case II), and logCa=-6.60 (Case III). The blue region represents the TCE, the gray region is water, and the white circles are solid grains.

Fig. 5 The flow fields in the original porous media and Case I-III. (a) The flow filed in the porous medium where is saturated by water; (b)-(d) The flow fields in Case I-III where the residual TCE varies the pore structure. The red color represents the residual TCE in Case I-III.

Fig. 6 The probability density functions (PDFs) of the longitudinal flow velocity and the flow velocity in the original porous media and Case I-III. (a) PDFs of longitudinal flow velocity in the original porous media and Case I-III. (b) PDFs of flow velocity in the original porous media and Case I-III.

844 **Fig. 7** The aqueous tracer transport in both the original aqueous porous media and
845 Case Ⅰ-Ⅲ (C/C_0 is the dimensionless concentration).

846 **Fig. 8** The breakthrough curves (BTCs) of the aqueous tracer transport in both the
847 original aqueous porous media and Case I-III.

848 **Fig. 9** Comparison the dispersivities from MIM and ADE models. The overall
849 dispersivity α_{MIM} was calculated with Eq. (19), the $\alpha_{L,ms}$ was determined by Eq.
850 (20), the dimensionless dispersivity index ϵ_d was obtained by Eq. (21)

851

852

853

854

855

856

857

858

859

860 **List of Table Captions**

861 **Table 1** Parameters of the aqueous flow fields in the original porous media and
862 Case I-III

863 **Table 2** Results from the goodness-of-fitting of the ADE and CTRW models

864 **Table 3** Summary of the parameters estimated from the MIM model

865

866

867

868

869

870

871

872

873

874

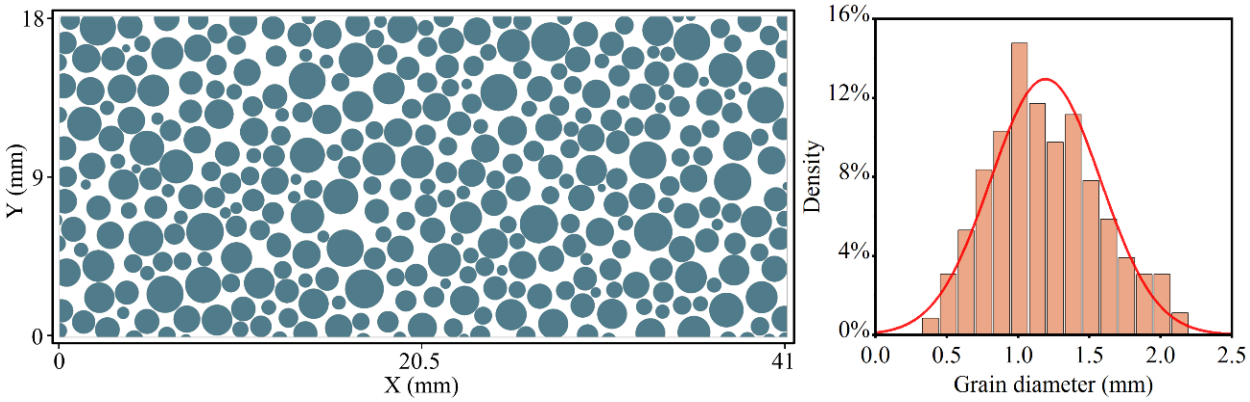

875

876 **Fig. 1** The generated porous medium and the distribution of grain diameter

877

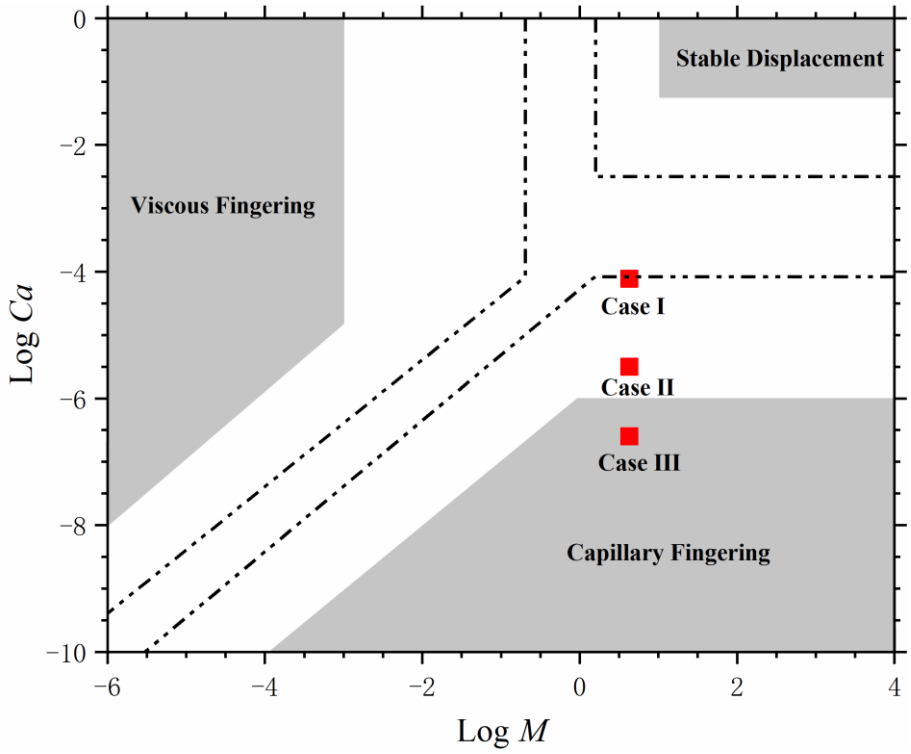

878

879 **Fig. 2** logCa - log$M$ phase diagram of the fluid-fluid displacement morphologies.
880 The viscous fingering, capillary fingering, and stable displacement zones bounded
881 by the black dash-dot line and the grey zone are obtained by [51] and [41],
882 respectively.

883

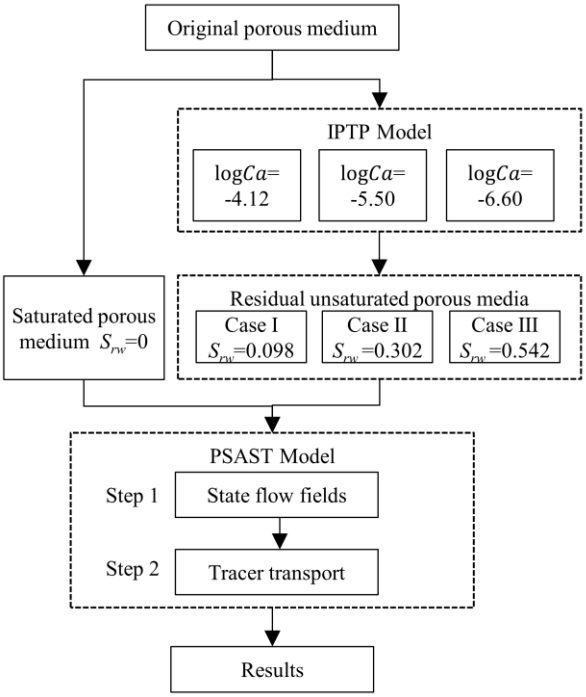

884

885 **Fig. 3** Flowchart of simulation

886

887

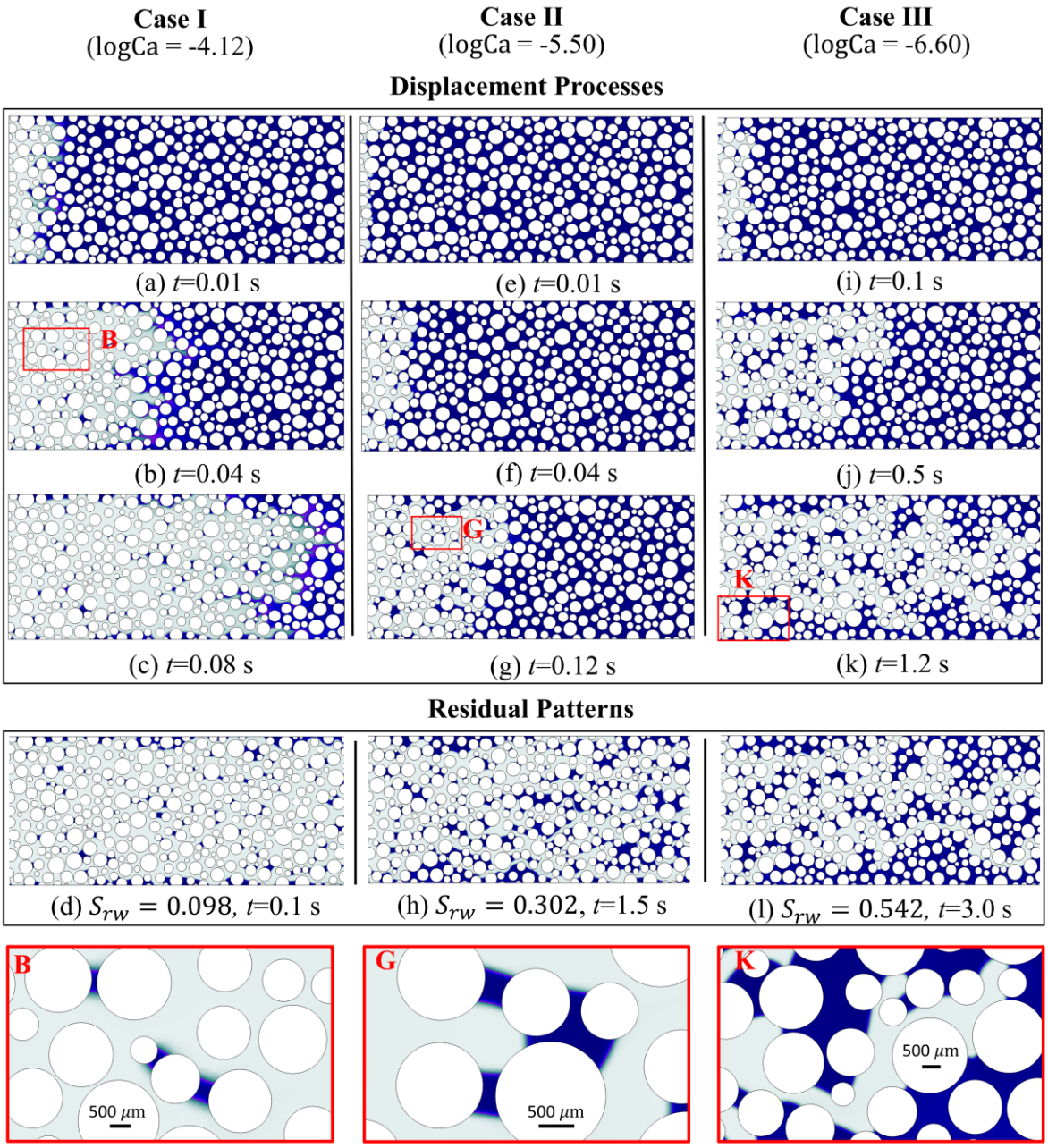

Fig. 4 Immiscible fluid-fluid displacement processes and residual patterns at logCa=-4.12 (Case I), logCa=-5.50 (Case II), and logCa=-6.60 (Case III). The blue region represents the TCE, the gray region is water, and the white circles are solid grains.

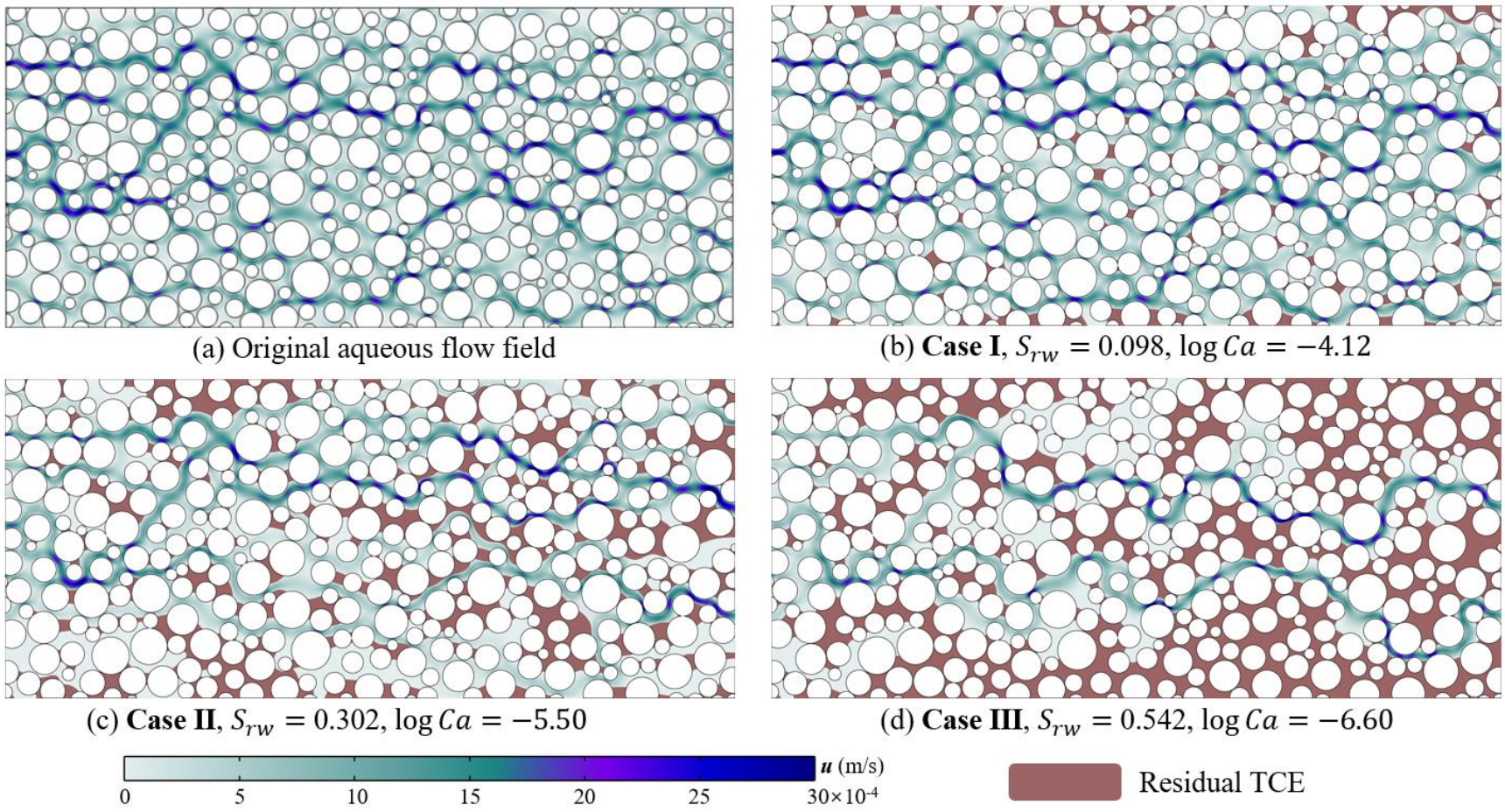

Fig. 5 The flow fields in the original porous media and Case I-III. (a) The flow filed in the porous medium where is saturated by water; (b)-(d) The flow fields in Case I-III where the residual TCE varies the pore structure. The red color represents the residual TCE in Case I-III.

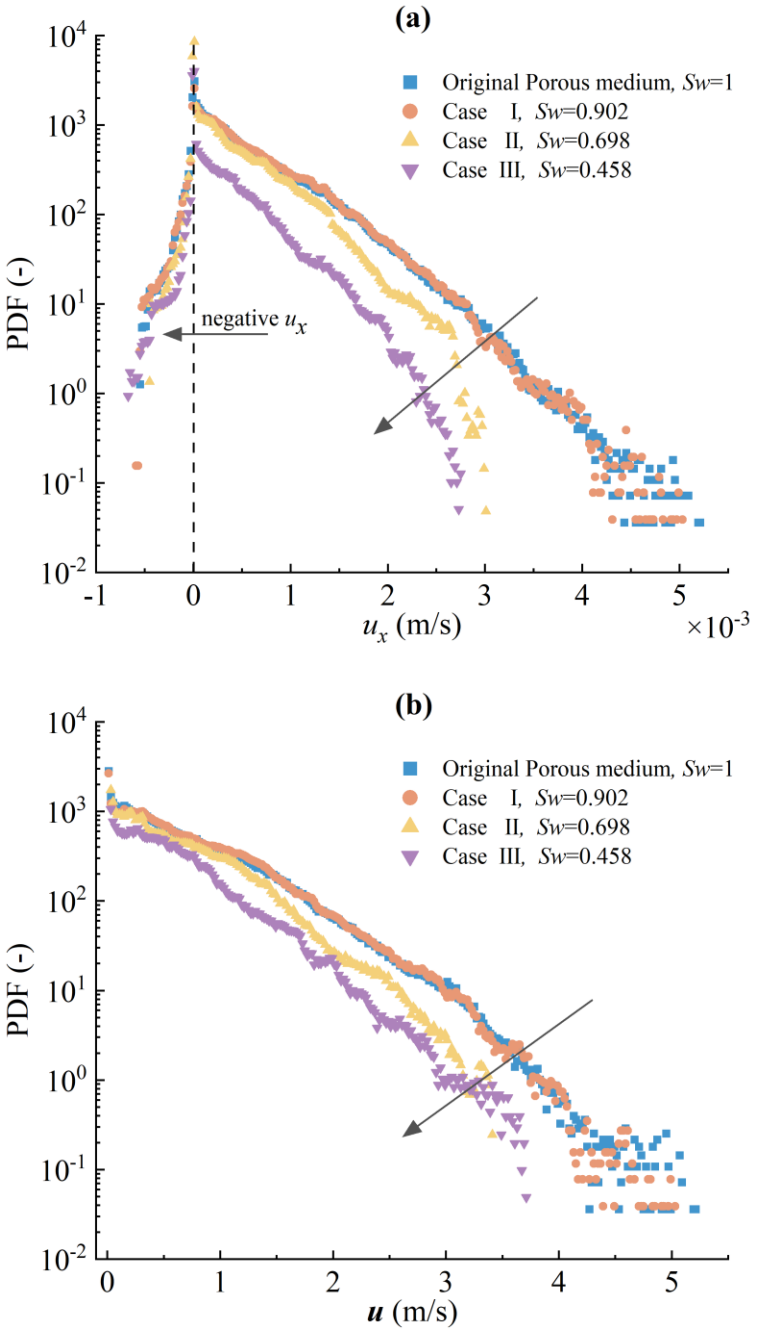

Fig. 6 The probability density functions (PDFs) of the longitudinal flow velocity and the flow velocity in the original porous media and Case I-III. (a) PDFs of longitudinal flow velocity in the original porous media and Case I-III. (b) PDFs of flow velocity magnitude in the original porous media and Case I-III.

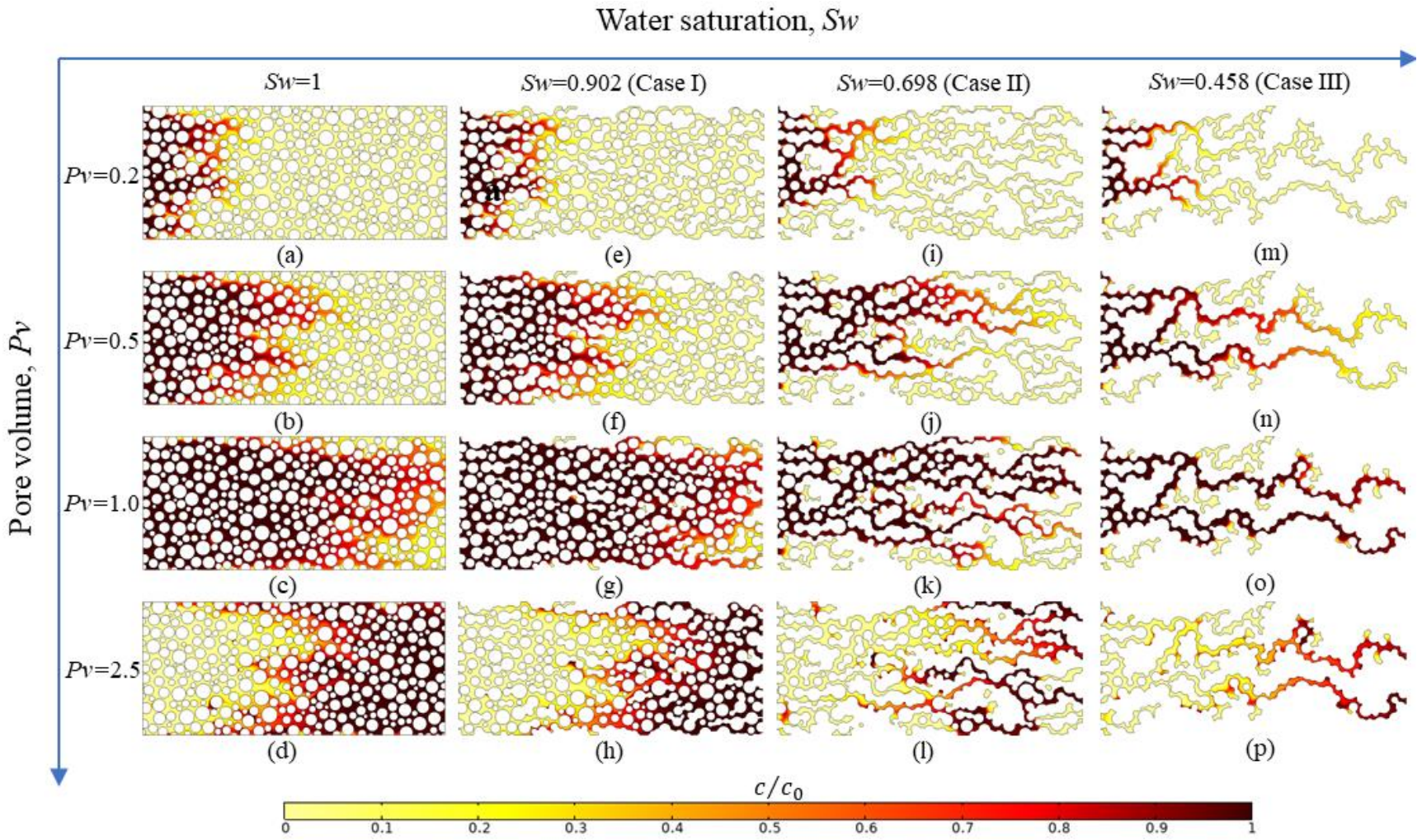

Fig. 7 The aqueous tracer transport in both the original aqueous porous media and Case I-III (C/C_0 is the dimensionless concentration).

907

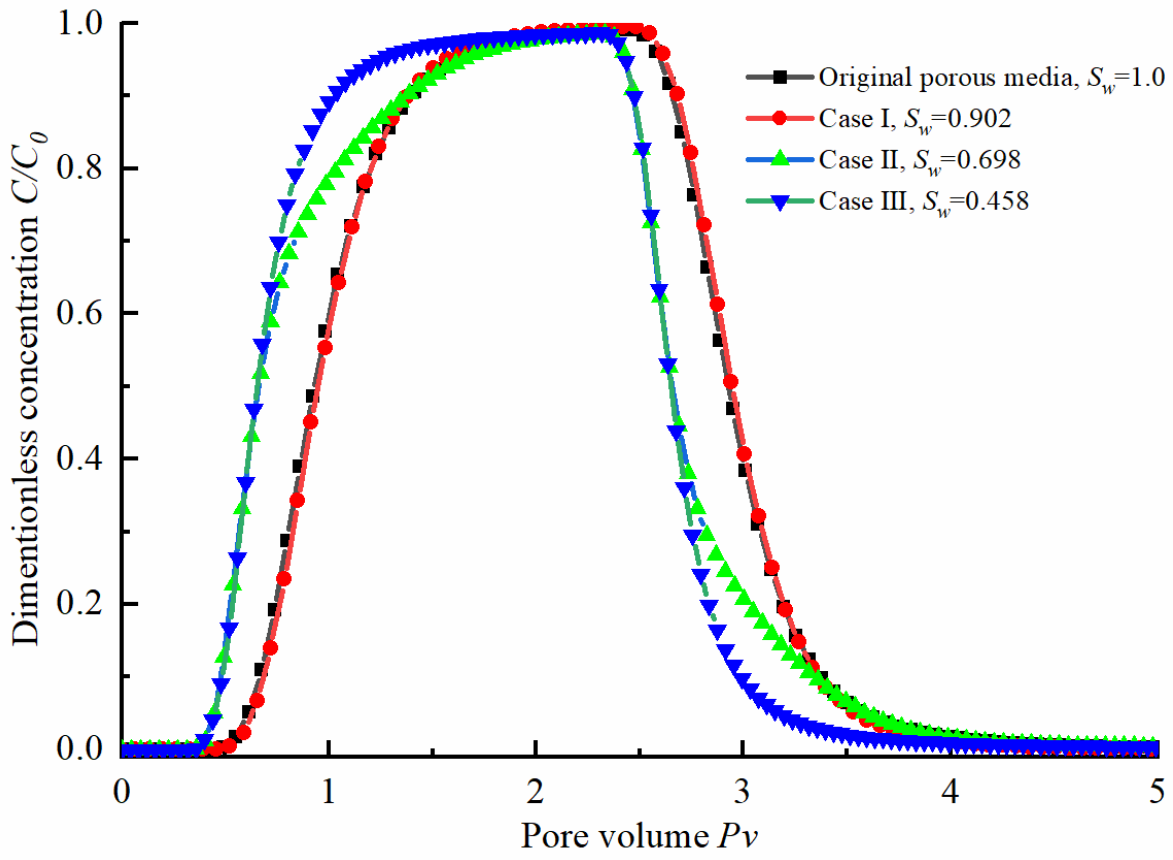

908

909 **Fig. 8** The breakthrough curves (BTCs) of the aqueous tracer transport in both the

910 original aqueous porous media and Case I-III.

911

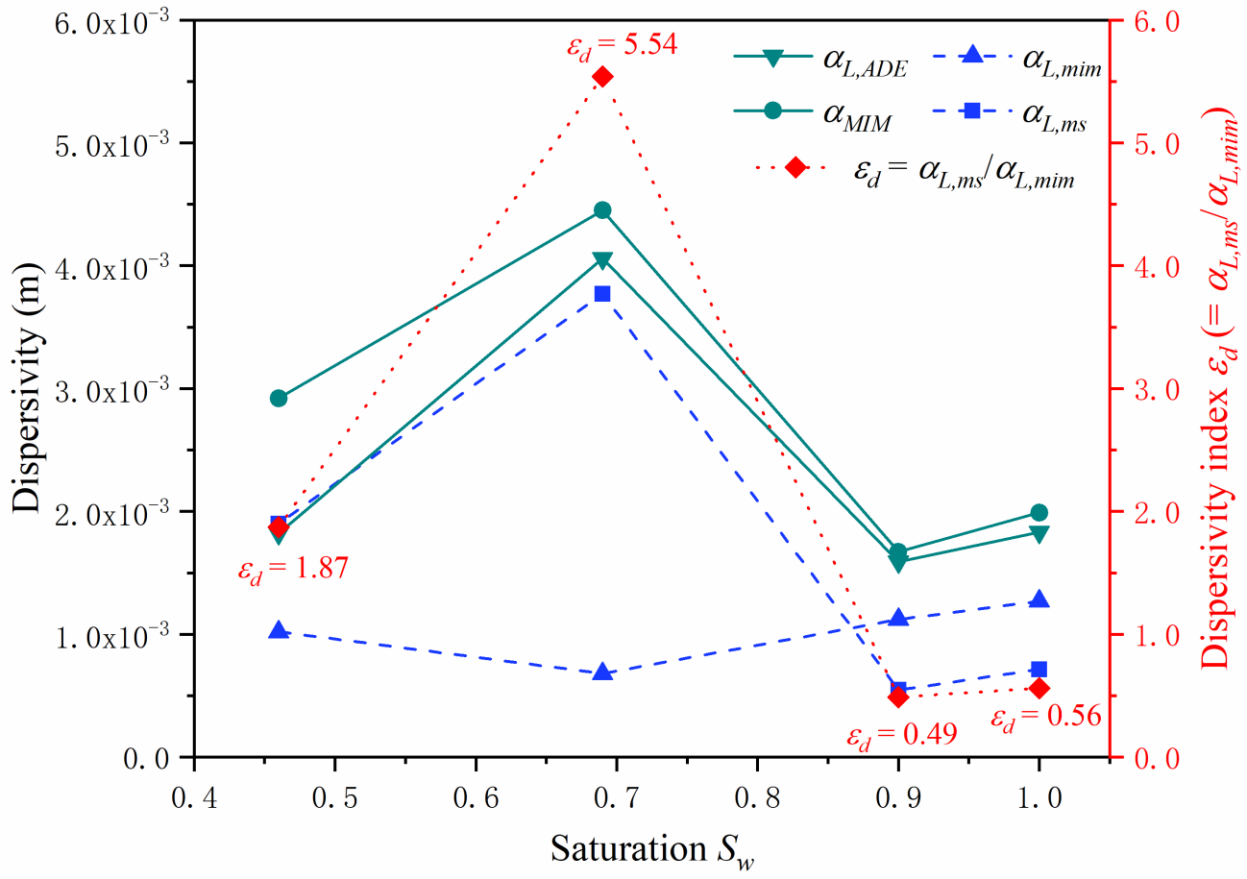

912

913 **Fig. 9** Comparison the dispersivities from MIM and ADE models. The overall

914 dispersivity α_{MIM} was calculated with Eq. (19), the $\alpha_{L,ms}$ was determined by Eq.

915 (20), the dimensionless dispersivity index ϵ_d was obtained by Eq. (21)

916

Table 1 Parameters of the aqueous flow fields in the original porous media and Case I-III

Porous Media	$\overline{u_x}$ (m/s)	$\bar{u}$ (m/s)	$\sigma^2_{(u)}$ (m^2/s^2)	$\sigma^2_{ln(u)}$ (-)	Pe (-)	Re (-)	CV_u (-)
Original ($S_w = 1.000$)	4.93×10^{-4}	6.30×10^{-4}	3.47×10^{-7}	3.79	393.87	0.39	0.89
Case I ($S_w = 0.902$)	5.26×10^{-4}	6.65×10^{-4}	3.45×10^{-4}	7.15	415.59	0.41	0.86
Case II ($S_w = 0.698$)	3.60×10^{-4}	4.61×10^{-4}	2.55×10^{-4}	58.40	287.97	0.29	1.19
Case III ($S_w = 0.458$)	3.25×10^{-4}	4.59×10^{-4}	2.03×10^{-4}	131.19	286.93	0.29	1.24

Note: $\overline{u_x}$ is the mean longitudinal flow velocity. $\sigma^2_{(u)}$ is the variance of the flow velocity. $\sigma^2_{ln(u)}$ is the natural logarithm of $\sigma^2_{(u)}$. *Pe* is dimensionless Peclet number. *Re* is dimensionless Reynolds number.

924

925

926 **Table 2** Results from the goodness-of-fitting of the ADE and CTRW models

Porous Media	ADE model					CTRW model							
	$\overline{u_{ADE}}$ (m/s)	D_{ADE} (m^2/s)	$\alpha_{L,ADE}$ (m)	E_i (-)	R^2 (-)	$\overline{u_{CTRW}}$ (m/s)	D_{CTRW} (m^2/s)	$\alpha_{L,CTRW}$ (m)	T_1 (s)	T_2 (s)	β_{CTRW} (-)	E_i (-)	R^2 (-)
Original ($S_w = 1.000$)	5.15×10^{-4}	9.40×10^{-7}	1.83×10^{-3}	0.009	0.999	5.17×10^{-4}	9.37×10^{-7}	1.81×10^{-3}	0.01	1405.72	1.91	0.016	0.999
Case I ($S_w = 0.902$)	5.42×10^{-4}	8.61×10^{-7}	1.59×10^{-3}	0.006	1.000	5.48×10^{-4}	8.43×10^{-7}	1.54×10^{-3}	0.01	1078.95	1.92	0.014	1.000
Case II ($S_w = 0.698$)	4.78×10^{-4}	1.94×10^{-7}	4.06×10^{-3}	0.030	0.994	4.82×10^{-4}	1.96×10^{-7}	4.07×10^{-3}	0.01	1120.73	1.80	0.030	0.990
Case III ($S_w = 0.458$)	4.74×10^{-4}	8.64×10^{-7}	1.82×10^{-3}	0.018	0.998	4.76×10^{-4}	8.72×10^{-7}	1.83×10^{-3}	0.01	968.95	1.90	0.023	0.998

927

928

929

930

931

932

933

934 **Table 3** Summary of the parameters estimated from the MIM model

Porous Media	$\overline{u_m}$ (m/s)	$D_{f,mim}$ (m^2/s)	β (-)	α (d^{-1})	$\alpha_{L,mim}$ (m)	R^2 (-)	E_i (-)
Original ($S_w = 1.000$)	5.55×10^{-4}	7.07×10^{-7}	0.93	1.63×10^{-3}	1.99×10^{-3}	0.999	0.006
Case I ($S_w = 0.902$)	5.89×10^{-4}	6.59×10^{-7}	0.92	2.36×10^{-3}	1.67×10^{-3}	0.999	0.005
Case II ($S_w = 0.698$)	6.50×10^{-4}	4.42×10^{-7}	0.74	2.59×10^{-3}	4.45×10^{-3}	0.998	0.018
Case III ($S_w = 0.458$)	5.28×10^{-4}	5.36×10^{-7}	0.90	5.10×10^{-4}	2.92×10^{-3}	0.999	0.016

935

936

937

938